Title

Real-Space Infrared Spectroscopy of Ferroelectric Domain Walls in Multiferroic h-(Lu,Sc)FeO3

Journal

ACS Applied Materials & Interfaces, 15(5)

ISSN

1944-8244

Authors

Smith, Kevin A

Ramkumar, Sriram P

Du, Kai

et al.

Publication Date

2023-02-08

DOI

10.1021/acsami.2c19600

Real space infrared spectroscopy of ferroelectric domain walls in multiferroic h-(Lu,Sc)FeO_3

Kevin A. Smith,[†] Sriram P. Ramkumar,[‡] Kai Du,[¶] Xianghan Xu,[¶] Sang-Wook Cheong,[¶,§] Stephanie N. Gilbert Corder,[‖] Hans A. Bechtel,[‖] Elizabeth A. Nowadnick,[‡] and Janice L. Musfeldt[*,†,⊥]

†*Department of Chemistry, University of Tennessee, Knoxville, Tennessee 37996, USA*

‡*Department of Materials Science and Engineering, University of California, Merced, California, 95343 USA*

¶*Department of Physics and Astronomy, Rutgers University, Piscataway, New Jersey 08854 USA*

§*Rutgers Center for Emergent Materials, Rutgers University, Piscataway, New Jersey 08854 USA*

‖*Advanced Light Source Division, Lawrence Berkeley National Laboratory, Berkeley, California 94720 USA*

⊥*Department of Physics and Astronomy, University of Tennessee, Knoxville, Tennessee 37996, USA*

E-mail: musfeldt@utk.edu

Abstract

We employ synchrotron-based near-field infrared spectroscopy to image the phononic properties of ferroelectric domain walls in hexagonal (h) $Lu_{0.6}Sc_{0.4}FeO_3$, and we compare our findings with a detailed symmetry analysis, lattice dynamics calculations, and prior models of domain wall structure. Rather than metallic and atomically thin

as observed in the rare earth manganites, ferroelectric walls in h-$Lu_{0.6}Sc_{0.4}FeO_3$ are broad and semiconducting, a finding that we attribute to the presence of an A-site substitution-induced intermediate phase that reduces strain and renders the interior of the domain wall non-polar. Mixed Lu:Sc occupation on the A site also provides compositional heterogeneity over micron-sized length scales, and we leverage the fact that Lu and Sc cluster in different ratios to demonstrate that the spectral characteristics at the wall are robust even in different compositional regimes. This work opens the door to broadband imaging of physical and chemical heterogeneity in ferroics and represents an important step to revealing the rich properties of these flexible defect states.

Keywords: ferroelectricity, domain walls, symmetry analysis, near field infrared imaging, orthoferrites

Introduction

Ferroelectric domain walls are usually considered to be atomically thin. There are numerous piezo-force and conducting atomic-force microscope measurements of hexagonal rare earth manganites demonstrating that the interlocked structural anti-phase and ferroelectric domain walls that combine to form cloverleaf-like vortices have essentially zero width.[1–6] As predicted by Fennie and Rabe,[7] improper ferroelectricity in the hexagonal rare earth manganites is induced by a Mn center buckling distortion.[8,9] The subsequent discovery of collective alternating net magnetization at cross-coupled domain walls[10,11] showed that interacting ferroelectric and magnetic domains (or walls) are key to understanding giant response mechanisms in many multiferroics. That walls have essentially zero width was verified theoretically by Kumagai and Spaldin[12] who studied two different models of domain walls in $YMnO_3$. The first was an atomically thin ferroelectric wall, and the second was a wider wall with an intermediate $P\bar{3}c1$ phase that effectively endows the interface with non-polar character. As the energy of the atomically-thin ferroelectric wall is lower than that of the wider, two-phase domain wall, we should anticipate ferroelectric domain walls of essentially zero width in the rare earth manganites and related materials.[12] While manganites are the archetype for fundamental studies of domain wall properties,[13] many other materials including complex chalcogenides,[14,15] lead perovskites,[16] and spin crossover complexes[17] host these structures, making it of great fundamental interest to image the phononic properties of these interfaces. At the same time, ferroelectric hafnia benefits from ultra-low barriers to topological domain wall switching[18] and wake-up and fatigue processes in $(Hf_{0.5}Zr_{0.5})O_2$ are connected with reversible domain wall transitions and oxygen center movement,[19] providing powerful reminders of the practical importance of these processes.

It is obviously quite challenging to image the properties of an interface with vanishing width. We therefore decided to explore a possible exception to this general case by taking advantage of the domain walls created by A-site substitution h-$Lu_{0.6}Sc_{0.4}FeO_3$.[20,21] Tunneling electron microscopy was utilized to map the ferroelectric domains previously, but unlike

infrared spectroscopy, it does not reveal the vibrational properties of domain walls. In addition to being a more suitable platform for our infrared imaging techniques, this system provides an opportunity to revisit predicted wall structures[12] and to explore precisely how local structure relaxes across a ferroelectric domain wall.

Ferrites generally adopt either an orthorhombic or hexagonal crystal symmetry depending on the radius of the A site ion.[22] $LuFeO_3$ normally hosts orthorhombic structure, although the pure hexagonal phase can be stabilized under epitaxial strain.[23] Similarly, A-site substitution with Sc, the smallest and lightest of the Group III elements, leads to a more compact lattice, which favors the hexagonal structure (Figure 1a). This is due to chemical pressure effects which give rise to local strain.[21,24] h-$Lu_{0.6}Sc_{0.4}FeO_3$ is ferroelectric at room temperature, providing ample opportunity to study ferroelectric domain walls at ambient conditions. At the same time, disorder and inhomogeneity are known to modify the overall width and number of domain walls.[25] Like the hexagonal rare earth manganites, h-$Lu_{0.6}Sc_{0.4}FeO_3$ is an improper ferroelectric with a polar distortion induced by buckling of the bipyramidal layers and Lu/Sc distortion in a trimerized fashion.[26,27] This system thus hosts two order parameters: the polar and so-called K_3 trimer distortions. Piezo-force microscopy reveals a cloverleaf pattern of micron-sized vortex ferroelectric domains in the single crystals[21] - similar to those in the manganites.[28] These ferroelectric domain walls are also structural antiphase boundaries due to rotating oxygen distortions.[21] Further analysis reveals two types of ferroelectric walls: one variety has FeO_5 dimers, and the other kind does not.[3] Low temperature magnetic force microscopy demonstrates that the weak ferromagnetic domains are distinct from the ferroelectric domains in terms of size and shape and that there exists no mutual locking between their domain walls.[21] These findings suggest decoupling between ferroelectricity and weak ferromagnetism in this system.[9] Domain walls have also been observed by scanning tunneling electron microscopy in related systems such as $(LuFeO_3)_m(LuFe_2O_4)_n$ superlattices.[29]

Although sensitive techniques have been developed for macroscopic measurements of

magnetoelectric coupling,[28,30] there remains a need to detect properties within a single domain or at a domain wall.[10,11,20] Vibrational spectroscopies are well-suited for unveiling the phonons that drive polar displacements in a ferroelectric material and exposing the microscopic origin of phononic properties such as thermal conductivity, specific heat, and thermal expansion.[31] As a reminder, ferroelectricity requires a broken inversion center, and infrared spectroscopy, with the ability to measure odd-symmetry vibrational modes, is the perfect method for revealing how symmetry evolves across a ferroelectric domain wall. Traditional infrared spectroscopy is not suitable because it cannot be focused beyond the diffraction limit $d = \lambda/2NA$, where λ is the wavelength of light, and NA is the size of the numerical aperture. This means that 500 cm^{-1} light has a diffraction-limited spot size of 10 μm or greater - far too large to image topological objects like domain walls. Synchrotron-based near-field infrared nano-spectroscopy offers a way forward as the 20 nm spatial resolution overcomes the diffraction limit and provides the sensitivity needed to measure samples with small lateral area.[32–34] Furthermore, the recent extension into the far infrared is ideal for complex oxides.[35] We recently employed this technique to explore strain relief and order parameter trends across ferroelastic walls in the hybrid improper ferroelectric $Ca_3Ti_2O_7$.[36] We imaged wide ferroelastic walls but were unable to resolve signatures of ferroelectric walls in crystals mapped with piezo-force microscopy, likely because they were too thin. Several related materials such as $Ca_3(Ti_{0.1}Ru_{0.9})_2O_7$ and $(Ca_{0.99}Sr_{0.01})_2RuO_4$ host ferroelastic domain walls with significant widths as well,[37,38] demonstrating that there are other systems of contemporary interest with macroscopic walls.

In order to advance the understanding of these fascinating topological defect states, we combine the wider ferroelectric domain walls in h-$Lu_{0.6}Sc_{0.4}FeO_3$ (induced by A-site substitution) with synchrotron-based near-field infrared nano-spectroscopy and compare our results with complementary lattice dynamics calculations and a symmetry analysis. Not only can we image the ferroelectric domain walls in this system for the first time, but we find that the structural relaxation is surprisingly wide - at least from a local structure point of

view. In addition to near-field amplitude changes across the walls, we detect small frequency shifts. We have long sought evidence for mode hardening and softening at both ferroelastic and ferroelectric walls, but in our prior work,[36] the predicted frequency shifts of the phonon modes were below our sensitivity. Now we can use these frequency shifts to revisit the question of whether there could be a non-polar structure embedded inside the ferroelectric wall[12] or whether the wall remains polar all the way through. We also take advantage of the natural compositional gradient due to *A*-site substitution to study wall behavior in slightly different chemical environments, providing an early glimpse of chemical tuning opportunities. This work opens the door to broadband imaging of physical and chemical heterogeneity in ferroics and represents an important step to revealing the rich properties of these flexible defect states for ultra-low power memory and computing devices.[39–41] More generally, Z_6 topological vortex domain structures are related to contemporary issues in quantum information (e.g. clock model, graph theory) as well as cosmology (the Kibble-Zurek mechanism which describes the possible formation of topological defects during a spontaneous symmetry breaking phase transition at the birth of the universe).[1,42,43] Physical manifestations of these models in the form of domain wall interfaces in ferroic oxides are therefore very attractive objects to explore.

Results and discussion

A-site substitution and compositional variation in the spectroscopic response

As a prelude to our near-field measurements of domain walls in *h*-$Lu_{0.6}Sc_{0.4}FeO_3$, we studied *A*-site substitution effects, the statistics of Lu and Sc occupation (best visualized as "red and blue balls" on 14 sites), and the impact of compositional heterogeneity on the spectroscopic response. By combining multiple techniques, we are able to place size constraints on the different compositional regions observed in *h*-$Lu_{0.6}Sc_{0.4}FeO_3$. This heterogeneity is

a consequence of the local structure and depends on the relative abundance of Lu and Sc (henceforth, the Lu:Sc ratio). What we find is that the global and local Lu:Sc ratios are different. The crystal structure of h-$Lu_{0.6}Sc_{0.4}FeO_3$ is shown in Figure 1a. It consists of a layer of corner-sharing FeO_5 bipyramids between the hexagonal slabs containing the Lu and Sc centers. We initially performed traditional infrared microscopy in order to understand the size of these compositional regions. Even using a 20 $\times$ 20 μm^2 aperture - close to the resolution limit for this method due to the diffraction limit of light - these measurements reveal no obvious differences. We therefore conclude that composition varies across much

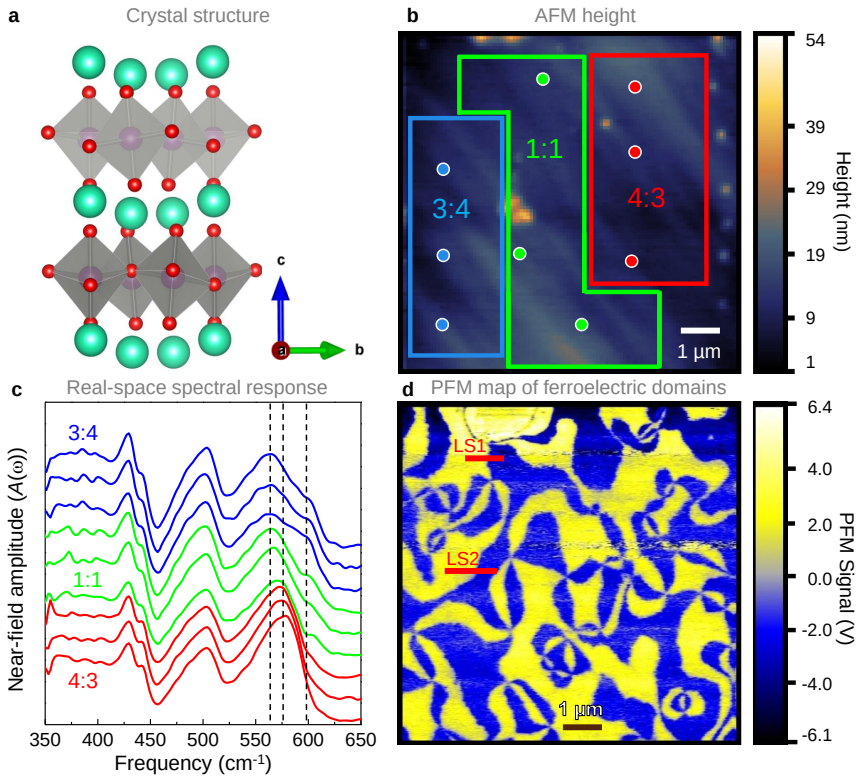

Figure 1: Overview of chemical and physical heterogeneity in h-$Lu_{0.6}Sc_{0.4}FeO_3$. (a) Crystal structure of the unit cell of h-$Lu_{0.6}Sc_{0.4}FeO_3$. The space group is $P6_3cm$.[21] Teal, purple and red spheres represent Lu/Sc sites, Fe atoms, and O atoms respectively. (b) Atomic force microscopy showing the topography of an area of interest with marks indicating the location of point spectra. (c) Point spectra corresponding to the locations indicated in (b). Curves are labeled and colored to match the different types of spectra observed in the various local composition areas. (d) Piezo-force microscopy of the ferroelectric vortex domains over the same area scanned in (b). Red lines show the positions of line scan 1 (LS1) and line scan 2 (LS2) taken in the 1:1 and 3:4 compositional regions, respectively.

smaller length scales. At the same time, we clearly observe different spectral responses using near-field techniques. Here, the spatial resolution is many orders of magnitude smaller (20 nm) due to the tip-enhanced nature of the method.[34] By sampling different areas on the surface, we are also able to identify different compositional regions which are significantly larger than the tip (Figure 1b). We therefore conclude that the compositional domains in h-$Lu_{0.6}Sc_{0.4}FeO_3$ are smaller than what can be measured with a far field technique but also larger than the spatial resolution of a near-field point scan. We estimate that the length scale of compositional variation is 1 - 3 microns (Figure 1b), similar to that other heterogeneous materials.[44] Moreover, each region hosts a slightly different spectroscopic response (Figure 1c). This mapping process allows topography and position be correlated with composition.

As established above, the spectral differences observed on the micron scale are due to the natural compositional variation in the sample. Because h-$Lu_{0.6}Sc_{0.4}FeO_3$ is stabilized in the hexagonal phase (as confirmed by x-ray diffraction), we know that the Lu:Sc ratio has to be between 4:3 and 3:4.[21] This implies that there are three principle compositional variants: 4:3, 1:1, and 3:4. On its surface, this is a standard case of understanding how A-site substitution and chemical inhomogeneity appear in and stabilize h-$Lu_{0.6}Sc_{0.4}FeO_3$. The distinguishing aspect of our work is how we combine this analysis with infrared imaging of the ferroelectric domain walls, linking both chemical and physical heterogeneity.

Due to the Lu vs. Sc mass difference, the Sc-rich rich areas display features at slightly higher frequencies. This general expectation explains the variations in Figure 1b,c and is justified by a detailed comparison of mode frequencies in $LuFeO_3$ vs. $ScFeO_3$ (Tables S1 and S2, Supporting Information). As a result, we can assign Lu:Sc ratios based upon the simplest models consistent with observed spectral shapes. Recall that there are three choices for crystals in the hexagonal phase: 4:3, 1:1, and 3:4. The spectra collected from the blue region in Figure 1b and plotted in Figure 1c displays the most prominent high frequency features. Specifically, the prominence of the peak at 600 cm^{-1}, which is primarily associated

with oxygen displacements calculated for $ScFeO_3$, is the key signature of this region, and we attribute it to the highest local Sc concentration and a Lu:Sc ratio of 3:4. Likewise, the region in green has prominent features at higher frequency when compared to the red area, so we assign the local Lu:Sc ratios in these regions as 1:1 and 4:3, respectively. We can therefore identify the local Lu:Sc ratio by subtle differences in the shape of the local near-field infrared response.

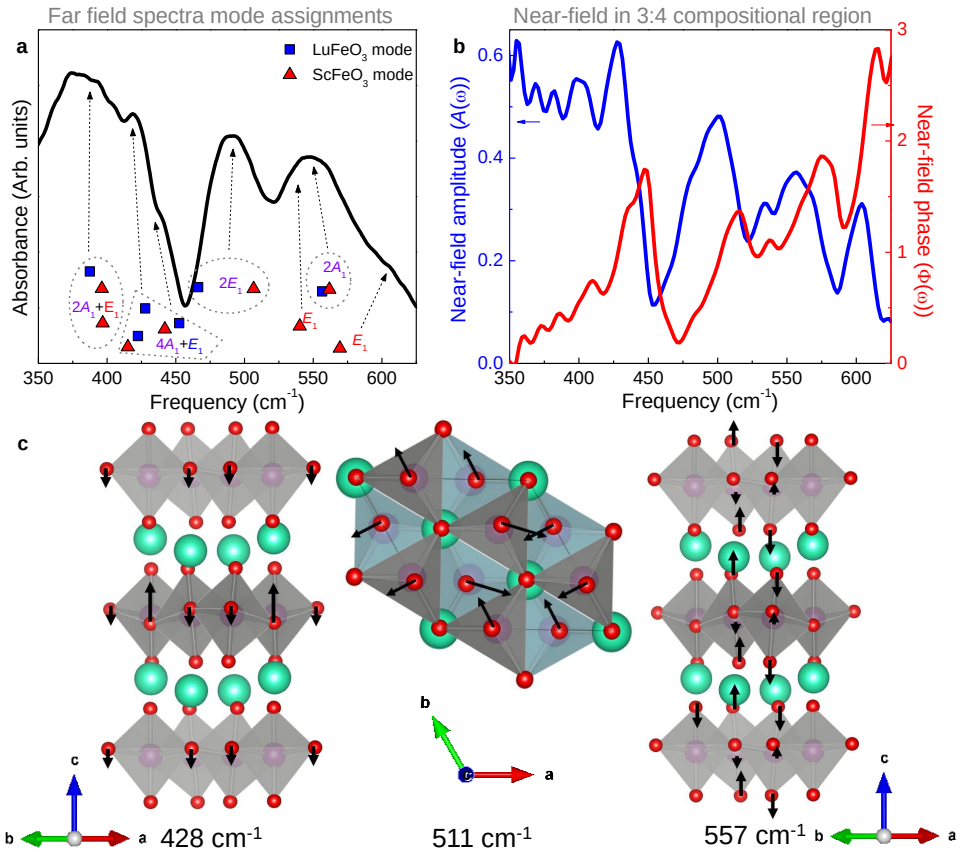

Figure 2: Comparison of far and near-field infrared spectra of h-$Lu_{0.6}Sc_{0.4}FeO_3$. (a) The far field infrared spectrum and (b) near-field amplitude and phase are in good agreement. We assign the features of the near-field spectrum based upon our complementary lattice dynamics calculations shown in (a). The theoretical modes are given by blue squares or red triangles for Lu- or Sc-containing modes, respectively. Both frequencies and relative intensities are indicated. This figure focuses on the frequency range of the near-field response. (c) Three selected mode displacement patterns (at 428, 511 and 557 cm^{-1}, computed for $LuFeO_3$). Displacement patterns calculated for $ScFeO_3$ are the same but with slightly higher frequency.

Vibrational mode assignments and lattice dynamics calculations

Figure 2 displays the absorption of h-$Lu_{0.6}Sc_{0.4}FeO_3$ measured by far field techniques, the synchrotron-based near-field infrared spectrum (both amplitude and phase), and the results of our complementary lattice dynamics calculations. We confine our attention to the region between 350 and 650 cm^{-1} where we have prominent features. Figure 2(c) shows representative phonon displacement patterns that occur near these frequencies. By inspecting displacement patterns, we find that phonons near 430 cm^{-1} have fairly complex patterns that combine bond stretching and bending. The mode at 428 cm^{-1} consists of primarily equatorial oxygen displacements, where within each bipyramid two oxygens displace down and the third displaces up by twice the amount (or two up, one down). This is somewhat reminiscent of the up-up-down A-site cation displacements found in these materials. The displacement patterns of phonons with frequencies near 510 cm^{-1} involve primarily bending of the Fe-O bonds, arising mainly from apical oxygen displacements. Finally, the phonons near 560 cm^{-1} consist mainly of Fe-O bond stretches. The vibrational modes that directly contain Lu and Sc motion as part of their displacement patterns resonate below 300 cm^{-1} - outside the range of the detector. On the other hand, the A site chemistry does provide indirect or "proximity effects" to the FeO_5-related stretching and bending modes as we discuss below. A full set of mode assignments including experimental + calculated frequencies and symmetries is given in the Supporting Information. With the mode assignments of h-$Lu_{0.6}Sc_{0.4}FeO_3$ on a firm foundation, we are ready to image the ferroelectric domain walls.

Near-field infrared imaging of ferroelectric domain walls

Beyond spectral changes due to compositional heterogeneity, h-$Lu_{0.6}Sc_{0.4}FeO_3$ hosts polar domains with ferroelectric walls that separate these domains. The walls in this system are unusually fat - probably due to A-site substitution. While having polarization "up" or "down" (Figure 1d) does not create spectral contrast in and of itself, there is infrared contrast at the interface. This is because symmetry is broken at the wall since polarization either has

to rotate (Néel wall) or turn off and on (Ising wall). Local compositional defects (such as oxygen deficiencies and perhaps the smaller Sc^{3+} ions) also tend to migrate to the walls.[45,46] In any case, the walls that we seek to image are extremely small, so a far field measurement with a large beam will provide only an average response.[47] Tip-enhanced techniques are needed to (i) beat the diffraction limit and (ii) reveal the properties of individual walls.

We locate ferroelectric domain walls of interest in h-$Lu_{0.6}Sc_{0.4}FeO_3$ with a multi-step procedure. We begin by measuring atomic- and piezo-force microscopy on a flat area of a crystal according to the natural topography present in both fields of view. The results of this process are provided in Figure 1b,d. Navigation is made easier by proximity to gold markers. In order to re-position ourselves near specific domain walls at the beamline, we perform additional atomic force microscopy to map the surface in the same field of view as previously mapped with piezo-force microscopy. This assures proper positioning of the tip for a near-field line scan. Details are available in the Methods and Supporting Information.

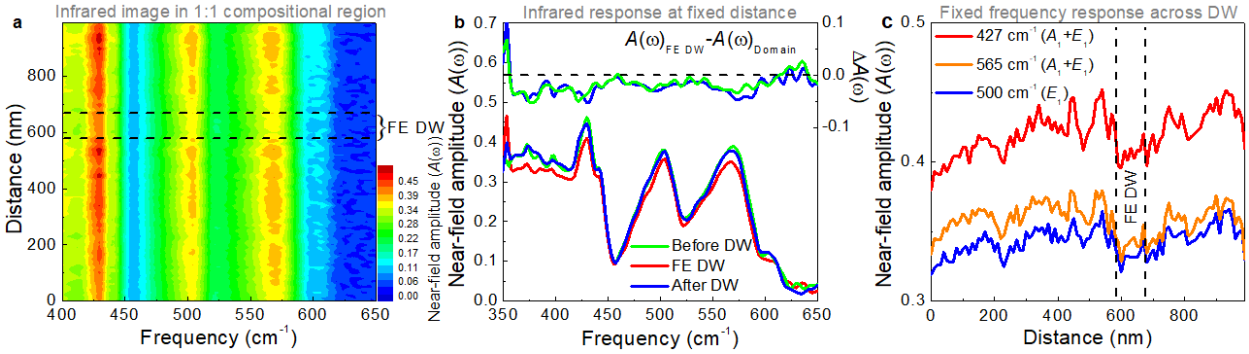

Figure 3: Near-field infrared response across a ferroelectric domain wall in h-$Lu_{0.6}Sc_{0.4}FeO_3$. (a) Color contour plot presents the near-field infrared response as a function of distance across a ferroelectric domain wall, indicated by the horizontal dashed lines, in the 1:1 Lu:Sc composition region. The image corresponds to line scan 1 in Figure 1d. The spatial resolution is 20×20 nm^2, and the spectrum is sampled every 10 nm along the line scan. The color indicates near-field amplitude as shown by the scale bar. (b) Constant distance curves, extracted from the real space infrared image in panel (a). Cuts are taken before, after, and at the ferroelectric domain wall. Difference spectra ($A(\omega)$ at the wall - $A(\omega)$ away from the wall) are shown at the top of this panel. (c) Fixed frequency cuts of the image in panel (a). These data reveal how the near-field amplitude evolves as a function of distance at the indicated frequencies which correspond to particular vibrational modes. The frequencies are selected to provide contrast at the ferroelectric domain wall in the 1:1 Lu:Sc compositional regime.

Figure 3 displays the real space infrared response of a ferroelectric domain wall taken wholly within the 1:1 Lu:Sc compositional domain of h-$Lu_{0.6}Sc_{0.4}FeO_3$ along with fixed position and fixed frequency cuts of the image. There are three primary findings. First, the phononic signature of the domain wall has lower near-field amplitude when compared to the surrounding area. Second, the extent of the spectral response spans roughly 100 nm, indicating that local structural aspects of the wall as measured by infrared spectroscopy are anomalously wide.[48–50] Third, the walls are semiconducting rather than metallic as evidenced by the strong phonon response and lack of a Drude signature. This is different than the conducting AFM results in the literature,[51–53] although several of the more recent studies emphasize that the region of the domain wall is simply more conducting than the surroundings rather than metallic.[20,54–58] We verify these findings by examining a ferroelectric domain wall in a different compositional region as described below.

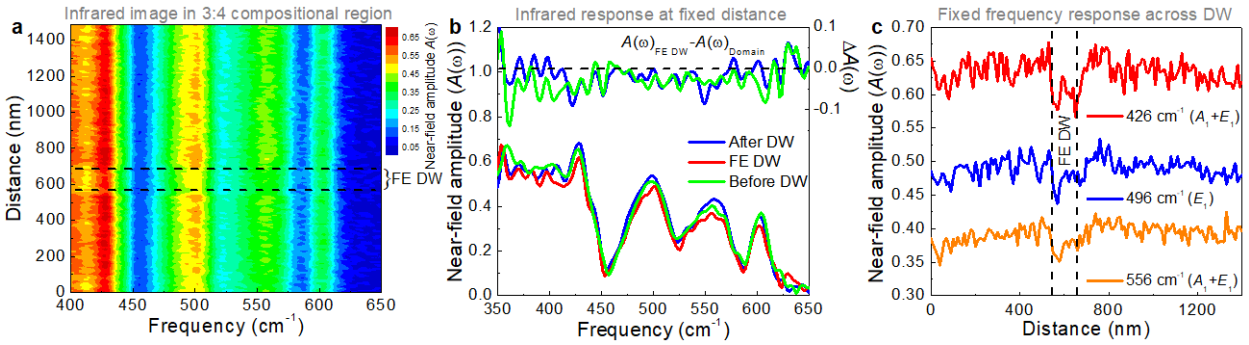

Figure 4: Near-field infrared response across a ferroelectric domain wall in h-$Lu_{0.6}Sc_{0.4}FeO_3$. (a) Color contour plot presents the near-field infrared response as a function of distance across a ferreoelectric domain wall, indicated by the horizontal dashed lines, in the 3:4 Lu:Sc composition region. The image corresponds to line scan 2 in Fig. 1(d). The spatial resolution is 20×20 nm^2, and the spectrum is sampled every 10 nm along the line scan. The color indicates near-field amplitude as shown by the scale bar. (b) Constant distance curves, extracted from the real space infrared image in panel (a). Cuts are taken before, after, and at the ferroelectric domain wall. Difference spectra ($A(\omega)$ at the wall - $A(\omega)$ away from the wall) are shown at the top of this panel. (c) Fixed frequency cuts of the image in panel (a). These data reveal how the near-field amplitude evolves as a function of distance at the indicated frequencies which correspond to particular vibrational modes. The frequencies are selected to provide contrast at the ferroelectric domain wall in the 3:4 Lu:Sc compositional region.

Figure 4 summarizes the synchroton-based near-field infrared response of a different fer-

roelectric domain wall. This one is fully within the 3:4 Lu:Sc compositional domain, and again it includes the contour plot as well as fixed position and fixed frequency cuts of the image. Certain similarities are immediately apparent, although there are significant differences as well. For instance, a line scan across the wall reveals clear phonons the entire time - an indication that the wall is insulating. The width of the wall in line scan 2 (120 nm) is slightly wider than in line scan 1, and again, we see diminished near-field amplitude at the wall. Because domain walls relieve strain between domains, energy is minimized if the system is allowed to relax over a wider range.[59,60] We attribute the width of the response to this relaxation.[36] This is different from the atomically thin walls reported previously.[48–50] We hypothesize that that Sc^{3+} (the small A site ion) and oxygen may be migrating to the defect,[61] thus creating larger distortions and broader structural relaxations.

Frequency shifts at the ferroelectric domain walls

In addition to amplitude and width changes, near-field infrared spectroscopy reveals that there are subtle frequency shifts of the phonon modes at the walls. While predicted in the past,[62,63] experimental evidence has been lacking - even though we have been searching for these signatures for some time. Resolving these changes is quite challenging because the expected frequency shifts are small, and the resolution that we employ in the near-field line scans (8 cm^{-1}) is traditionally not very high. As a result, the frequency shifts that we find in h-$Lu_{0.6}Sc_{0.4}FeO_3$ are at the limit of our sensitivity. Even so, frequency shifts are observed in nearly all of the phonons - both bending and stretching modes. Figure 5 summarizes our findings.

Focusing first on the bending modes of h-$Lu_{0.6}Sc_{0.4}FeO_3$, we see that wall phonons are nearly identical to those in the nearby ferroelectric domains. For instance, none of the O–Fe–O bending modes shift at the wall in the 1:1 or 3:4 Lu:Sc composition regimes. The Fe–O stretching modes are more interesting. The response of the wall in the 3:4 Lu:Sc region is

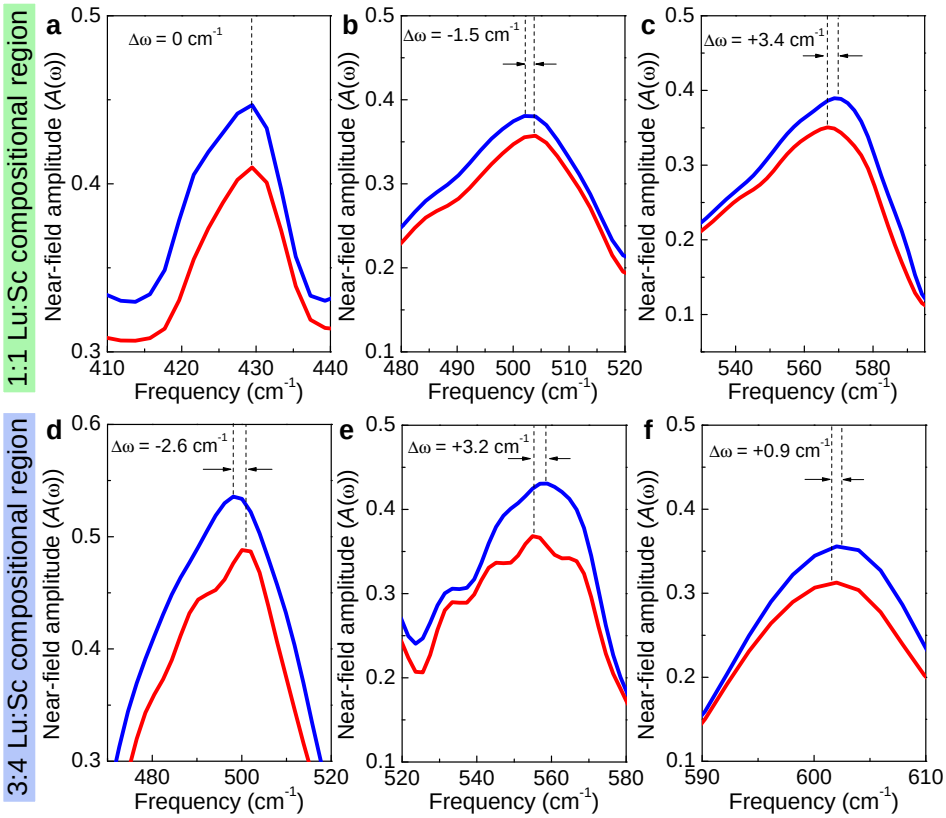

Figure 5: Close-up view of the frequency shifts at the ferroelectric domain walls. (a-c) Data are taken within the 1:1 Lu:Sc compositional region and (d-f) are taken from the 3:4 Lu:Sc compositional region. Data are taken at (red curves) and away from (blue curves) the domain wall to emphasize the frequency shifts associated with the wall.

the most significant with frequency shifts on the order of -2.6, +3.2, and +0.9 cm^{-1} for the stretching modes near 498, 559, and 602 cm^{-1}, respectively. These are significant frequency shifts suggesting the possibility that the ferroelectric domain walls in the 3:4 Lu:Sc compositional region of h-$Lu_{0.6}Sc_{0.4}FeO_3$ may have a different internal structure than the surroundings - akin to the higher energy structure proposed by Kumagai and Spaldin in Ref. [12]. While these frequency shifts are not precise enough to tease out the intermediate space group inside the domain wall as we have done with h-$Lu_{0.6}Sc_{0.4}FeO_3$ under pressure,[27] they are consistent with the overall picture of using a structural modification to minimize strain across a relatively wide wall. Frequency shifts of the 504 and 568 cm^{-1} Fe–O stretching modes at the wall in the 1:1 Lu:Sc composition region are also significant at -1.5 and

+3.4 cm^{-1}, respectively. If these frequency shifts could be augmented by near-field data at lower frequencies, it might be possible to compare calculations of the hexagonal, $P\bar{3}c1$, and $P6_3/mmc$ structures to see if predicted frequency shifts across the wall are consistent with the measurements. Such a comparison could, in principle, reveal the nature of an intermediate phase that might allow a wide domain wall to host a non-polar interior. Finally, we point out that based upon these frequency shifts, the force constants change by 1 or 2% at the interface. Both softening and hardening is observed.

Conclusions

In this work, we combined synchrotron-based near-field infrared nano-spectroscopy, a detailed symmetry analysis, and lattice dynamics calculations to reveal the properties of a quasi-one-dimensional topological object in the form of a ferroelectric domain wall. These studies are enabled by development of broad band infrared imaging with nanometer-scale spatial resolution and the fat domain walls in $Lu_{0.6}Sc_{0.4}FeO_3$ where, thanks to A-site substitution, we also explore how local stoichiometry variations impact the response. Contrary to the expectation for atomically sharp conducting domain walls, we find semiconducting walls with wide local lattice distortions that act to minimize strain. Further, phonon frequency shifts across the ferroelectric domain walls are consistent with the appearance of an intermediate (possibly non-polar) phase internal to the wall, in line with models studied by Kumagai and Spaldin.[12] Looking ahead, ferroelectric domain walls of the type discussed in this work will find application in emerging logic and memory technologies. Naturally, properties like thermal conductivity and heat capacity are key to effective heat management, and useful microscopic models of dissipation require information about the fundamental excitations of the lattice at the wall in addition to wall-induced scattering.[64] These findings open the door to phononic engineering of domain wall-based device architectures where strategies to create bespoke behavior by altering local chemistry significantly extend the complexity of these

efforts.

Methods

Crystal growth, characterization, and mapping: High-quality h-$Lu_{0.6}Sc_{0.4}FeO_3$ single crystals were grown using optical floating zone techniques as described previously.[21] X-ray diffraction was used to confirm the hexagonal phase, and the lack of peak broadening confirmed the quality of the single crystals.[21] We mounted the crystal to expose the ab-plane surface for microscopy measurements and used gold markers to determine location. Both atomic force and piezo-force microscopies were performed at room temperature to associate surface topology with the shape and position of the polar domains. We located each region of interest using this gold marker-topological-polar domain map and selected near-field line scans to cross features of interest as described below. For all the piezo-force microscopy measurements, 5 V AC at 68 kHz was applied to a tip (a commercial conductive AFM tip) while the sample backside was grounded. We also employed near-field infrared spectroscopy to explore the chemical heterogeneity in h-$Lu_{0.6}Sc_{0.4}FeO_3$ and delineate compositional boundaries. These images were overlaid with topography and polarity information to perform line scans within different compositional ranges.

Synchrotron-based near-field spectroscopic techniques: near-field infrared measurements were carried out at Beamline 2.4 of the Advanced Light Source at Lawrence Berkeley National Laboratory.[34,35] Here, a commercial Neaspec NeaSNOM instrument is coupled to a customized Ge:Cu detector with a KRS5 or Si beamsplitter (330 - 800 cm^{-1}; 8 cm^{-1} resolution).[35] A PtSi tip with 25 nm radius is used to achieve the 20 $\times$ 20 nm^2 spatial resolution. Second harmonic near-field amplitude $A(\omega)$ and phase $\Phi(\omega)$ are obtained simultaneously. We focus primarily on the near-field amplitude as it is most strongly related to traditional reflectance. Line scans of various lengths were carried out in order to cross between different polar domains and, by so doing, traverse a ferroelectric wall. Spectra were sampled every 10

nm on each line scan. By oversampling in real space, we improve the spatial resolution and signal-to-noise ratios. The area of interest is mapped with atomic force microscopy before and after each line scan to check for sample drift. All of these experiments were done at room temperature.

Traditional far field infrared spectroscopy: Complementary far field measurements were performed using a suite of spectrometers in our lab (including a Bruker 113v Fourier transform infrared spectrometer equipped with a helium-cooled bolometer and an Equinox 55 equipped with an attached infrared microscope) over the 20 - 7,000 cm^{-1} frequency range. Far field spectroscopy was used to confirm the spectral shape and mode assignments. It was also employed to place constraints on the size of the compositional domains in *h*-$Lu_{0.6}Sc_{0.4}FeO_3$. Spatial resolution of the infrared microscope is on the order of 20 $\times$ 20 μm^2 - several orders of magnitude larger that of our near-field measurements. This difference is used to support our analysis of chemical heterogeneity.

Density functional theory calculations: We performed density functional theory (DFT) calculations using the projector augmented wavemethod as implemented in VASP[65] on the end-member compounds $LuFeO_3$ and $ScFeO_3$. To treat the electronic correlations on Fe, we employed the Liechtenstein *et al.*[66] formulation of DFT+U, with on-site Coulomb and exchange parameters U=4.5 eV and J=0.95 eV. An A-type antiferromagnetic (A-AFM) order was imposed on the Fe spins. We used the PBEsol functional a 600 eV plane-wave energy cutoff, and a 4×4×2 Γ-centered k-point mesh. For structural relaxations, forces are converged to 2 meV/Å. We used density functional perturbation theory (DFPT)[67] to compute the Γ-point phonon frequencies, Born effective charge tensors ($Z^*_{\kappa,\alpha\beta}$ for atom κ and displacement directions $\alpha, \beta = 1, 2, 3$), and eigendisplacements ($X_{\kappa,\beta}$). Using these quantities, we calculated the infrared intensity of phonon mode m using PHONOPY[68,69] and the

Phonopy-Spectroscopy package:[70]

$$I_{IR}(m) = \sum_{\alpha} \Big| \sum_{\kappa} \sum_{\beta} Z^{*}_{\kappa,\alpha\beta} X_{\kappa,\beta}(m) \Big|^2. \quad (1)$$

Phonon assignments are made taking into account both the phonon frequency as well as the infrared intensity given by Equation 1. We note that the phonon frequencies of $LuFeO_3$ and $ScFeO_3$ are slightly different (Tables S1 and S2 Supporting Information) due to the different ionic sizes of the Lu and Sc cations. We expect the phonon frequencies in $Lu_{0.6}Sc_{0.4}FeO_3$ to lie between those of the two end member compounds.

Supporting Information: Calculated phonon frequencies for the $P6_3mc$ phase of $LuFeO_3$ and $ScFeO_3$ (Tables S1 and S2), detailed explanation of sample mapping (Figure S1), and investigation of domain wall conductance (Figure S2)

Acknowledgments: Research at the University of Tennessee is supported by the Division of Materials Research at the National Science Foundation (DMR-2129904). The Advanced Light Source is supported by the Office of Basic Energy Sciences, Division of Materials Sciences and Engineering, of the U.S. Department of Energy under Contract No. DE-AC02-05CH11231. The work at Rutgers was supported by the center for Quantum Materials Synthesis (cQMS), funded by the Gordon and Betty Moore Foundation's EPiQS initiative through grant GBMF10104, and by Rutgers University. This research used resources of the Scientific Data and Computing Center, a component of the Computational Science Initiative, at Brookhaven National Laboratory, funded under Contract No. DE-SC0012704, U. S. DoE.

Author contributions: This project was conceived by JLM and SWC. The single crystals were grown and AFM + PFM mapping studies were carried out by KD and XX with advice from SWC.. The spectroscopic work was performed by KAS with assistance from SGC, HAB, and JLM. The first principles electronic structure calculations were carried out by SPR with guidance from EAN. Data analysis was completed by KAS with advice from JLM. All authors discussed the findings. The manuscript was written by KAS and JLM. All

authors read and commented on the manuscript.

References

(1) Chae, S. C.; Horibe, Y.; Jeong, D. Y.; Rodan, S.; Lee, N.; Cheong, S.-W. Self-Organization, Condensation, and Annihilation of Topological Vortices and Antivortices in a Multiferroic. *Proceedings of the National Academy of Sciences* **2010**, *107*, 21366–21370.

(2) Jungk, T.; Hoffmann, Á.; Fiebig, M.; Soergel, E. Electrostatic Topology of Ferroelectric Domains in $YMnO_3$. *Applied Physics Letters* **2010**, *97*, 012904.

(3) Choi, T.; Horibe, Y.; Yi, H. T.; Choi, Y. J.; Wu, W.; Cheong, S.-W. Insulating Interlocked Ferroelectric and Structural Antiphase Domain Walls in Multiferroic $YMnO_3$. *Nature Materials* **2010**, *9*, 253–258.

(4) Meier, D.; Seidel, J.; Cano, A.; Delaney, K.; Kumagai, Y.; Mostovoy, M.; Spaldin, N. A.; Ramesh, R.; Fiebig, M. Anisotropic Conductance at Improper Ferroelectric Domain Walls. *Nature Materials* **2012**, *11*, 284–288.

(5) Seidel, J. Domain Walls as Nanoscale Functional Elements. *The Journal of Physical Chemistry Letters* **2012**, *3*, 2905–2909.

(6) Han, M.-G.; Zhu, Y.; Wu, L.; Aoki, T.; Volkov, V.; Wang, X.; Chae, S. C.; Oh, Y. S.; Cheong, S.-W. Ferroelectric Switching Dynamics of Topological Vortex Domains in a Hexagonal Manganite. *Advanced Materials* **2013**, *25*, 2415–2421.

(7) Fennie, C. J.; Rabe, K. M. Ferroelectric Transition in $YMnO_3$ from First Principles. *Physical Review B* **2005**, *72*, 100103.

(8) Van Aken, B. B.; Palstra, T. T.; Filippetti, A.; Spaldin, N. A. The Origin of Ferroelectricity in Magnetoelectric $YMnO_3$. *Nature Materials* **2004**, *3*, 164–170.

(9) Artyukhin, S.; Delaney, K. T.; Spaldin, N. A.; Mostovoy, M. Landau Theory of Topological Defects in Multiferroic Hexagonal Manganites. *Nature Materials* **2014**, *13*, 42–49.

(10) Geng, Y.; Lee, N.; Choi, Y. J.; Cheong, S.-W.; Wu, W. Collective Magnetism at Multiferroic Vortex Domain Walls. *Nano Letters* **2012**, *12*, 6055–6059.

(11) Geng, Y.; Das, H.; Wysocki, A. L.; Wang, X.; Cheong, S.-W.; Mostovoy, M.; Fennie, C. J.; Wu, W. Direct Visualization of Magnetoelectric Domains. *Nature Materials* **2014**, *13*, 163–167.

(12) Kumagai, Y.; Spaldin, N. A. Structural Domain Walls in Polar Hexagonal Manganites. *Nature Communications* **2013**, *4*, 1540.

(13) Evans, D. M.; Garcia, V.; Meier, D.; Bibes, M. Domains and Domain Walls in Multiferroics. *Physical Sciences Reviews* **2020**, *5*, 20190067.

(14) Sun, Q.-C.; Song, T.; Anderson, E.; Brunner, A.; Förster, J.; Shalomayeva, T.; Taniguchi, T.; Watanabe, K.; Gräfe, J.; Stöhr, R.; Xu, X.; Wrachtrup, J. Magnetic Domains and Domain Wall Pinning in Atomically Thin $CrBr_3$ Revealed by Nanoscale Imaging. *Nature Communications* **2021**, *12*, 1989.

(15) Alliati, I. M.; Evans, R. F. L.; Novoselov, K. S.; Santos, E. J. G. Relativistic Domain-Wall Dynamics in Van der Waals Antiferromagnet $MnPS_3$. *npj Computational Materials* **2022**, *8*, 3.

(16) Zhang, H.-Y.; Song, X.-J.; Chen, X.-G.; Zhang, Z.-X.; You, Y.-M.; Tang, Y.-Y.; Xiong, R.-G. Observation of Vortex Domains in a Two-Dimensional Lead Iodide Perovskite Ferroelectric. *Journal of the American Chemical Society* **2020**, *142*, 4925–4931.

(17) Jakobsen, V. B.; Trzop, E.; Gavin, L. C.; Dobbelaar, E.; Chikara, S.; Ding, X.; Esien, K.; Müller-Bunz, H.; Felton, S.; Zapf, V. S.; Collet, E.; Carpenter, M. A.; Morgan, G. G.

Stress-Induced Domain Wall Motion in a Ferroelastic Mn^{3+} Spin Crossover Complex. *Angewandte Chemie* **2020**, *132*, 13407–13414.

(18) Choe, D.-H.; Kim, S.; Moon, T.; Jo, S.; Bae, H.; Nam, S.-G.; Lee, Y. S.; Heo, J. Unexpectedly Low Barrier of Ferroelectric Switching in HfO_2 via Topological Domain Walls. *Materials Today* **2021**, *50*, 8–15.

(19) Cheng, Y.; Gao, Z.; Ye, K. H.; Park, H. W.; Zheng, Y.; Zheng, Y.; Gao, J.; Park, M. H.; Choi, J.-H.; Xue, K.-H.; Hwang, C. S.; Lyu, H. Reversible Transition Between the Polar and Antipolar Phases and its Implications for Wake-Up and Fatigue in HfO_2-Based Ferroelectric Thin Film. *Nature Communications* **2022**, *13*, 645.

(20) Wu, X.; Du, K.; Zheng, L.; Wu, D.; Cheong, S.-W.; Lai, K. Microwave Conductivity of Ferroelectric Domains and Domain Walls in a Hexagonal Rare-Earth Ferrite. *Physical Review B* **2018**, *98*, 081409.

(21) Du, K.; Gao, B.; Wang, Y.; Xu, X.; Kim, J.; Hu, R.; Huang, F.-T.; Cheong, S.-W. Vortex Ferroelectric Domains, Large-Loop Weak Ferromagnetic Domains, and Their Decoupling in Hexagonal (Lu, Sc)FeO_3. *npj Quantum Materials* **2018**, *3*, 33.

(22) White, J.; Sinha, K.; Xu, X. Structural Phase Diagram and Magnetic Properties of Sc-Substituted Rare Earth Ferrites $R_{1-x}Sc_xFeO_3$ (R = Lu, Yb, Er, and Ho). *Journal of Applied Physics* **2019**, *125*, 244101.

(23) Sinha, K.; Zhang, Y.; Jiang, X.; Wang, H.; Wang, X.; Zhang, X.; Ryan, P. J.; Kim, J.-W.; Bowlan, J.; Yarotski, D. A.; Li, Y.; DiChiara, A. D.; Cheng, X.; Wu, X.; Xu, X. Effects of Biaxial Strain on the Improper Multiferroicity in $LuFeO_3$ Films Studied Using the Restrained Thermal Expansion Method. *Physical Review B* **2017**, *95*, 094110.

(24) Disseler, S. M.; Luo, X.; Gao, B.; Oh, Y. S.; Hu, R.; Wang, Y.; Quintana, D.; Zhang, A.; Huang, Q.; Lau, J.; Paul, R.; Lynn, J. W.; Cheong, S.-W.; Ratcliff, W. Multiferroicity in Doped Hexagonal $LuFeO_3$. *Physical Review B* **2015**, *92*, 054435.

(25) Oh, Y. S.; Luo, X.; Huang, F.-T.; Wang, Y.; Cheong, S.-W. Experimental Demonstration of Hybrid Improper Ferroelectricity and the Presence of Abundant Charged Walls in $(Ca,Sr)_3Ti_2O_7$ Crystals. *Nature Materials* **2015**, *14*, 407–413.

(26) Sinha, K.; Wang, H.; Wang, X.; Zhou, L.; Yin, Y.; Wang, W.; Cheng, X.; Keavney, D. J.; Cao, H.; Liu, Y.; Wu, X.; Xu, X. Tuning the Néel Temperature of Hexagonal Ferrites by Structural Distortion. *Physical Review Letters* **2018**, *121*, 237203.

(27) Smith, K. A.; Ramkumar, S. P.; Harms, N. C.; Clune, A. J.; Cheong, S.-W.; Liu, Z.; Nowadnick, E. A.; Musfeldt, J. L. Pressure-Induced Phase Transition and Phonon Softening in h-$Lu_{0.6}Sc_{0.4}FeO_3$. *Physical Review B* **2021**, *104*, 094109.

(28) Wu, X.; Petralanda, U.; Zheng, L.; Ren, Y.; Hu, R.; Cheong, S.-W.; Artyukhin, S.; Lai, K. Low-Energy Structural Dynamics of Ferroelectric Domain Walls in Hexagonal Rare-Earth Manganites. *Science Advances* **2017**, *3*, e1602371.

(29) Holtz, M. E.; Padgett, E. S.; Steinhardt, R.; Brooks, C. M.; Meier, D.; Schlom, D. G.; Muller, D. A.; Mundy, J. A. Dimensionality-Induced Change in Topological Order in Multiferroic Oxide Superlattices. *Physical Review Letters* **2021**, *126*, 157601.

(30) Leiner, J. C.; Kim, T.; Park, K.; Oh, J.; Perring, T. G.; Walker, H. C.; Xu, X.; Wang, Y.; Cheong, S.-W.; Park, J.-G. Magnetic Excitations in the Bulk Multiferroic Two-Dimensional Triangular Lattice Antiferromagnet (Lu, Sc)FeO_3. *Physical Review B* **2018**, *98*, 134412.

(31) Fan, S.; Singh, S.; Xu, X.; Park, K.; Qi, Y.; Cheong, S. W.; Vanderbilt, D.; Rabe, K. M.; Musfeldt, J. L. Vibrational Fingerprints of Ferroelectric HfO_2. *npj Quantum Materials* **2022**, *7*, 32.

(32) Muller, E. A.; Pollard, B.; Raschke, M. B. Infrared Chemical Nano-Imaging: Accessing Structure, Coupling, and Dynamics on Molecular Length Scales. *The Journal of Physical Chemistry Letters* **2015**, *6*, 1275–1284.

(33) Mastel, S.; Govyadinov, A. A.; Maissen, C.; Chuvilin, A.; Berger, A.; Hillenbrand, R. Understanding the Image Contrast of Material Boundaries in IR Nanoscopy Reaching 5 nm Spatial Resolution. *ACS Photonics* **2018**, *5*, 3372–3378.

(34) Bechtel, H. A.; Johnson, S. C.; Khatib, O.; Muller, E. A.; Raschke, M. B. Synchrotron Infrared Nano-Spectroscopy and -Imaging. *Surface Science Reports* **2020**, *75*, 100493.

(35) Khatib, O.; Bechtel, H. A.; Martin, M. C.; Raschke, M. B.; Carr, G. L. Far Infrared Synchrotron Near-Field Nanoimaging and Nanospectroscopy. *ACS Photonics* **2018**, *5*, 2773–2779.

(36) Smith, K. A.; Nowadnick, E. A.; Fan, S.; Khatib, O.; Lim, S. J.; Gao, B.; Harms, N. C.; Neal, S. N.; Kirkland, J. K.; Martin, M. C.; Won, C. J.; Raschke, M. B.; Cheong, S.-W.; Fennie, C. J.; Carr, G. L.; Bechtel, H. A.; Musfeldt, J. L. Infrared Nano-Spectroscopy of Ferroelastic Domain Walls in Hybrid Improper Ferroelectric $Ca_3Ti_2O_7$. *Nature Communications* **2019**, *10*, 5235.

(37) McLeod, A. S.; Wieteska, A.; Chiriaco, G.; Foutty, B.; Wang, Y.; Yuan, Y.; Xue, F.; Gopalan, V.; Chen, L. Q.; Mao, Z. Q.; Millis, A. J.; Pasupathy, A. N.; Basov, D. N. Nano-Imaging of Strain-Tuned Stripe Textures in a Mott Crystal. *npj Quantum Materials* **2021**, *6*, 46.

(38) Vitalone, R. A.; Sternbach, A. J.; Foutty, B. A.; McLeod, A. S.; Sow, C.; Golez, D.; Nakamura, F.; Maeno, Y.; Pasupathy, A. N.; Georges, A.; Millis, A. J.; Basov, D. N. Nanoscale Femtosecond Dynamics of Mott Insulator $(Ca_{0.99}Sr_{0.01})_2RuO_4$. *Nano Letters* **2022**, *22*, 5689–5697.

(39) Roy, K. Ultra-Low-Energy Non-Volatile Straintronic Computing Using Single Multiferroic Composites. *Applied Physics Letters* **2013**, *103*, 173110.

(40) Mittal, S. A Survey of Techniques for Approximate Computing. *ACM Computing Surveys* **2016**, *48*, 1–33.

(41) Royo, M.; Escorihuela-Sayalero, C.; Íñiguez, J.; Rurali, R. Ferroelectric Domain Wall Phonon Polarizer. *Physical Review Materials* **2017**, *1*, 051402.

(42) Zurek, W. H. Cosmological Experiments in Superfluid Helium? *Nature* **1985**, *317*, 505–508.

(43) Duong, D. L.; Han, G. H.; Lee, S. M.; Gunes, F.; Kim, E. S.; Kim, S. T.; Kim, H.; Ta, Q. H.; So, K. P.; Yoon, S. J.; Chae, S. J.; Jo, Y. W.; Park, M. H.; Chae, S. H.; Lim, S. C.; Choi, J. Y.; Lee, Y. H. Probing Graphene Grain Boundaries with Optical Microscopy. *Nature* **2012**, *490*, 235–239.

(44) Hao, Z.; Bechtel, H. A.; Kneafsey, T.; Gilbert, B.; Nico, P. S. Cross-Scale Molecular Analysis of Chemical Heterogeneity in Shale Rocks. *Scientific Reports* **2018**, *8*, 2552.

(45) Eliseev, E. A.; Morozovska, A. N.; Kalinin, S. V.; Li, Y.; Shen, J.; Glinchuk, M. D.; Chen, L.-Q.; Gopalan, V. Surface Effect on Domain Wall Width in Ferroelectrics. *Journal of Applied Physics* **2009**, *106*, 084102.

(46) Guzelturk, B.; Mei, A. B.; Zhang, L.; Tan, L. Z.; Donahue, P.; Singh, A. G.; Schlom, D. G.; Martin, L. W.; Lindenberg, A. M. Light-Induced Currents at Domain Walls in Multiferroic $BiFeO_3$. *Nano Letters* **2020**, *20*, 145–151.

(47) Sun, Q.-C.; Xi, X.; Wang, X.; Lee, N.; Mazumdar, D.; Smith, R. J.; Carr, G. L.; Cheong, S.-W.; Musfeldt, J. L. Spectroscopic Signatures of Domain Walls in Hexagonal $ErMnO_3$. *Physical Review B* **2014**, *90*, 121303.

(48) Chrosch, J.; Salje, E. K. H. Temperature Dependence of the Domain Wall Width in $LaAlO_3$. *Journal of Applied Physics* **1999**, *85*, 722–727.

(49) Catalan, G.; Seidel, J.; Ramesh, R.; Scott, J. F. Domain Wall Nanoelectronics. *Reviews of Modern Physics* **2012**, *84*, 119–156.

(50) Moreno, R.; Evans, R. F. L.; Khmelevskyi, S.; Muñoz, M. C.; Chantrell, R. W.; Chubykalo-Fesenko, O. Temperature-Dependent Exchange Stiffness and Domain Wall Width in Co. *Physical Review B* **2016**, *94*, 104433.

(51) Seidel, J.; Martin, L. W.; He, Q.; Zhan, Q.; Chu, Y.-H.; Rother, A.; Hawkridge, M. E.; Maksymovych, P.; Yu, P.; Gajek, M.; Balke, N.; Kalinin, S. V.; Gemming, S.; Wang, F.; Catalan, G.; Scott, J. F.; Spaldin, N. A.; Orenstein, J.; Ramesh, R. Conduction at Domain Walls in Oxide Multiferroics. *Nature Materials* **2009**, *8*, 229–234.

(52) Seidel, J.; Maksymovych, P.; Batra, Y.; Katan, A.; Yang, S.-Y.; He, Q.; Baddorf, A. P.; Kalinin, S. V.; Yang, C.-H.; Yang, J.-C.; Chu, Y.-H.; Salje, E. K. H.; Wormeester, H.; Salmeron, M.; Ramesh, R. Domain Wall Conductivity in La-Doped $BiFeO_3$. *Physical Review Letters* **2010**, *105*, 197603.

(53) Maksymovych, P.; Seidel, J.; Chu, Y. H.; Wu, P.; Baddorf, A. P.; Chen, L.-Q.; Kalinin, S. V.; Ramesh, R. Dynamic Conductivity of Ferroelectric Domain Walls in $BiFeO_3$. *Nano Letters* **2011**, *11*, 1906–1912.

(54) Guyonnet, J.; Gaponenko, I.; Gariglio, S.; Paruch, P. Conduction at Domain Walls in Insulating $Pb(Zr_{0.2}Ti_{0.8})O_3$ Thin Films. *Advanced Materials* **2011**, *23*, 5377–5382.

(55) Stolichnov, I.; Feigl, L.; McGilly, L. J.; Sluka, T.; Wei, X.-K.; Colla, E.; Crassous, A.; Shapovalov, K.; Yudin, P.; Tagantsev, A. K.; Setter, N. Bent Ferroelectric Domain Walls as Reconfigurable Metallic-Like Channels. *Nano Letters* **2015**, *15*, 8049–8055.

(56) Liu, L.; Xu, K.; Li, Q.; Daniels, J.; Zhou, H.; Li, J.; Zhu, J.; Seidel, J.; Li, J. Giant Domain Wall Conductivity in Self-Assembled $BiFeO_3$ Nanocrystals. *Advanced Functional Materials* **2021**, *31*, 2005876.

(57) Bartels, M.; Hagen, V.; Burianek, M.; Getzlaff, M.; Bismayer, U.; Wiesendanger, R. Impurity-Induced Resistivity of Ferroelastic Domain Walls in Doped Lead Phosphate. *Journal of Physics: Condensed Matter* **2003**, *15*, 957–962.

(58) Vasudevan, R. K.; Wu, W.; Guest, J. R.; Baddorf, A. P.; Morozovska, A. N.; Eliseev, E. A.; Balke, N.; Nagarajan, V.; Maksymovych, P.; Kalinin, S. V. Domain Wall Conduction and Polarization-Mediated Transport in Ferroelectrics. *Advanced Functional Materials* **2013**, *23*, 2592–2616.

(59) Tagantsev, A. K.; Cross, L. E.; Fousek, J. *Domains in Ferroic Crystals and Thin Films*; Springer New York: New York, NY, 2010.

(60) Yudin, P. V.; Gureev, M. Y.; Sluka, T.; Tagantsev, A. K.; Setter, N. Anomalously Thick Domain Walls in Ferroelectrics. *Physical Review B* **2015**, *91*, 060102.

(61) Xu, T.; Shimada, T.; Araki, Y.; Wang, J.; Kitamura, T. Multiferroic Domain Walls in Ferroelectric $PbTiO_3$ With Oxygen Deficiency. *Nano Letters* **2016**, *16*, 454–458.

(62) Seijas-Bellido, J. A.; Escorihuela-Sayalero, C.; Royo, M.; Ljungberg, M. P.; Wojdeł, J. C.; Íñiguez, J.; Rurali, R. A Phononic Switch Based on Ferroelectric Domain Walls. *Physical Review B* **2017**, *96*, 140101.

(63) Yelisieiev, M.; Maksymovych, P.; Morozovska, A. N. Probing Phonon Softening in Ferroelectrics by Scanning Probe Microwave Spectroscopy. *Physical Review B* **2021**, *104*, 174105.

(64) Bugallo, D.; Langenberg, E.; Ferreiro-Vila, E.; Smith, E. H.; Stefani, C.; Batlle, X.; Catalan, G.; Domingo, N.; Schlom, D. G.; Rivadulla, F. Deconvolution of Phonon Scattering by Ferroelectric Domain Walls and Point Defects in a $PbTiO_3$ Thin Film Deposited in a Composition-Spread Geometry. *ACS Applied Materials Interfaces* **2021**, *13*, 45679–45685.

(65) Kresse, G.; Furthmüller, J. Efficiency of Ab-Initio Total Energy Calculations for Metals and Semiconductors Using a Plane-Wave Basis Set. *Comp. Mater. Sci.* **1996**, *6*, 15–50.

(66) Liechtenstein, A. I.; Anisimov, V. I.; Zaanen, J. Density-Functional Theory and Strong Interactions: Orbital Ordering in Mott-Hubbard Insulators. *Phys. Rev. B* **1995**, *52*, R5467–R5470.

(67) Gonze, X.; Lee, C. Dynamical Matrices, Born Effective Charges, Dielectric Permittivity Tensors, and Interatomic Force Constants From Density-Functional Perturbation Theory. *Physical Review B* **1997**, *55*, 10355–10368.

(68) Togo, A.; Oba, F.; Tanaka, I. First-Principles Calculations of the Ferroelastic Transition Between Rutile-Type and $CaCl_2$-Type SiO_2 at High Pressures. *Physical Review B* **2008**, *78*, 134106.

(69) Togo, A.; Chaput, L.; Tanaka, I. Distributions of Phonon Lifetimes in Brillouin Zones. *Physical Review B* **2015**, *91*, 094306.

(70) Skelton, J. M.; Burton, L. A.; Jackson, A. J.; Oba, F.; Parker, S. C.; Walsh, A. Lattice Dynamics of the Tin Sulphides SnS_2, SnS and Sn_2S_3: Vibrational Spectra and Thermal Transport. *Physical Chemistry Chemical Physics* **2017**, *19*, 12452–12465.